AAM: AN ASSESSMENT METRIC OF AXIAL CHROMATIC ABERRATION

Majed El Helou, Frederike Dümbgen, Sabine Süsstrunk

School of Computer and Communication Sciences, EPFL, Lausanne, Switzerland

ABSTRACT

Knowledge of lens specifications is important to identify the best lens for a given capture scenario and application. Lens manufacturers provide many specifications in their data sheets, and multiple initiatives for testing and comparing different lenses can be found online. However, due to the lack of a suitable metric or technique, no evaluation of axial chromatic aberration is available.

In this paper, we propose a metric, Axial Aberration Magnitude or AAM, that assesses the degree of axial chromatic aberration of a given lens. Our metric is generalizable to multispectral acquisition systems and is very simple and cheap to compute. We present the entire procedure and algorithm for computing the AAM metric, and evaluate it for two spectral systems and two consumer lenses.

Index Terms— Axial chromatic aberration, lens assessment metric, chromatic aberration blur.

1. INTRODUCTION

Chromatic aberration is present in all camera systems to different extents. Chromatic aberrations are caused by dispersion, as the refractive index of a lens is non-linearly wavelength dependent. Every acquired wavelength λ has a different refractive index $n(\lambda)$ and is thus deviated by a different angle [1, 2]. The result is that every wavelength has its own focal length $f(\lambda)$ and power $P(\lambda)$ given by the *lens makers' formula* [3]:

$$P(\lambda) = \frac{1}{f(\lambda)} = (n(\lambda) - 1)\left(\frac{1}{\epsilon_1} - \frac{1}{\epsilon_2}\right), \qquad (1)$$

making it focus at a different distance from the lens whose curvature radii are ϵ_1 and ϵ_2. As this leads to discrepancies in image focus across different channels and to color fringing, lens manufacturers attempt to correct for chromatic aberration by aligning multiple lens elements with complementary dispersion properties. This leads to three general categories of lenses defined by their chromatic correction, namely apochromatic, achromatic and superachromatic, the latter being designed to also correct for near-infrared (NIR) wavelengths up to 1000 nm [1, p. 105].

Chromatic aberration has undesirable visual artifacts [4–6], and can be a challenge to multispectral applications where spatial matching between channels is important [7]. However, it can also be useful in deblurring for multispectral systems having acquisition channels with shifted focus depth [2, 8, 9] by transferring high frequencies from one channel to another.

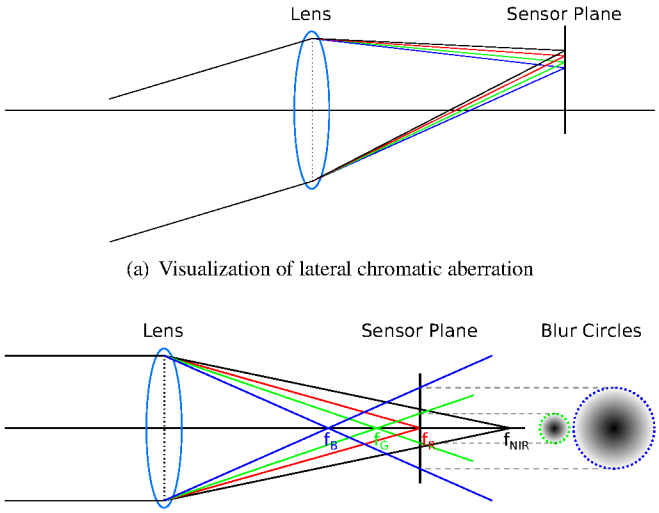

(a) Visualization of lateral chromatic aberration

(b) Visualization of axial chromatic aberration, with green and blue blur circles

Fig. 1. Behind the lens, black rays correspond to NIR, and colored rays correspond to their own colors. (a) Lateral chromatic aberration causes color fringing, due to shifted blur circles across the sensor. (b) Axial chromatic aberration seen as different blur radius sizes for different spectral channels.

Chromatic aberrations are either axial (longitudinal) or lateral (transverse) chromatic aberrations (Fig. 1). Axial chromatic aberration is best visualized by the difference in blur radii on the sensor plane of two incident rays of different wavelengths along the optical axis of the lens. It causes color spilling with different degrees depending on the wavelength. Lateral chromatic aberration is the dispersion of rays arriving obliquely to the lens, mostly seen around the edges of an image and causing color fringing.

Considerable effort has been and is still being extended to understand axial chromatic aberration in the human visual system [10–13]. However, a metric for camera systems is still lacking. As stated in their documentation, quality assessment solutions such as *imatest* [14] or *DxOMark* [15] can evaluate lateral aberration on standard ISO charts or dot charts, respectively, but not axial aberration. Due to the lack of an

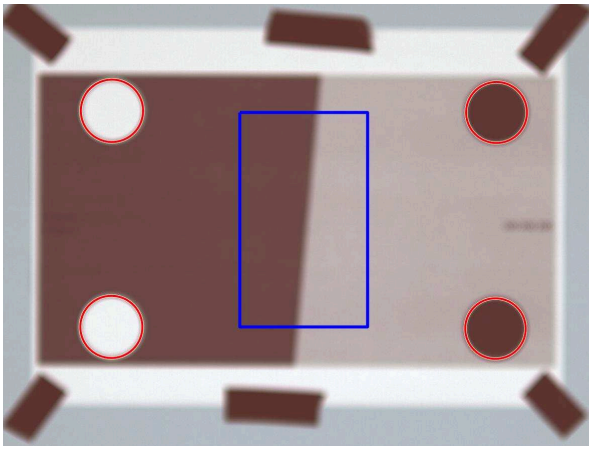

Fig. 2. One out-of-focus image of our slanted edge target. By detecting the four disks, we delimit a central region that only contains the slanted edge and extract it for processing.

evaluation metric for the latter, lens reviewers and photographers have no means to assess and compare lenses based on the magnitude of their axial chromatic aberration.

In this paper, we propose a novel metric called Axial Aberration Magnitude (AAM). This metric is designed to be simple, reproducible and generalizable to multispectral system evaluation. It is parametrized to assess axial chromatic aberration magnitude for different depth ranges of interest. The AAM computes the magnitude of the point spread function (PSF) as a function of depth and compares its deviation across the captured spectral channels. A simple slanted edge printed using a regular printer suffices to compute the AAM of a lens, since what is of importance are the relative blur magnitudes between spectral channels and not the absolute per-channel sharpness performance.

Section 2 presents the acquisition details to obtain all the data needed to compute the AAM. Section 3 discusses the mathematical foundation of the AAM metric. Section 4 explains the full procedure and links between practice and the theory developed in Section 3. And lastly, results on two commercial lenses are reported in Section 5.

2. DATA ACQUISITION

An essential objective is to make the AAM metric easily reproducible. We rely on inexpensive hardware, simple setups and codes and data used in this paper are made publicly available[1].

To evaluate the degree of axial chromatic aberration of a lens, a comparison of PSFs in different spectral channels needs to be conducted across a range of depth (camera-to-scene distance). For a simple yet realistic metric, we follow the assumption of a symmetric Gaussian PSF [16–21]. To estimate the scale of the PSF, we take pictures of an A4 paper with a sharp slanted edge oriented at 5 degrees away from the vertical. The sharp edge is created between two almost black and white regions; we use more greyish colors to avoid potential camera sensor saturation that might affect the assessment. Four disks are also printed symmetrically on the borders of the paper to automate the localization of the edge region. The camera is stabilized on a tripod. We vary the distance separating the slanted edge and the camera, as described in Section 4, thus capturing a sequence of images. Then, we detect the four disks in every image to localize the paper and delimit the region of interest in which only the slanted edge is visible. Acquisition is carried out under the illumination of two reflector-equipped light sources, positioned symmetrically at 45-degree angles (to the left and right sides of the camera) to reduce specular reflections.

With the extracted edge data, we follow the ISO 12233 procedure [22] to obtain edge spread functions (ESF). We compute the ESF for every image at every depth, but also for every spectral channel. We differentiate the obtained ESFs along the horizontal dimension to get the corresponding line spread functions (LSF). With the assumption of a symmetric PSF, we only need to evaluate the PSF scale in one direction, horizontally in our case, thus the vertical slanted edge is enough to estimate the scale of the PSF. Each LSF is then fitted to a one-dimensional Gaussian distribution, from which we retain the standard deviation as a measure of scale. We finally obtain, as a function of object-camera distance, PSF scale values for every spectral channel. The PSF curves can be seen in Fig. 3 for two different lenses, and for the red (R), green (G), blue (B) and near-infrared (NIR) spectral channels. These PSF curves are analyzed in Section 3 to compute the AAM metric for a given lens and set of multispectral channels.

3. MATHEMATICAL FOUNDATION

We denote the PSF radius in channel Λ_i by r_i, where $r_i(x)$ is the radius at scene depth x. The radius for a given distance is estimated in practice as the standard deviation of a Gaussian distribution fitted to the LSF, as explained in Section 2. This can be done because both variables are directly proportional. The difference $\delta_\alpha(\Lambda_i, \Lambda_j)$ between two PSF radii curves in two channels Λ_i and Λ_j is computed as the norm of the difference between the curves in question:

$$\begin{aligned}\delta_\alpha(\Lambda_i, \Lambda_j) &= ||r_i - r_j||^2 = \langle r_i - r_j, r_i - r_j \rangle \\ &= \int_{a_{ij}}^{b_{ij}} [r_i(x) - r_j(x)]^2 dx,\end{aligned} \tag{2}$$

and the integral limits are given by:

$$\begin{cases} a_{ij} = (1-\alpha) * min(x_i^0, x_j^0) \\ b_{ij} = (1+\alpha) * max(x_i^0, x_j^0), \end{cases} \tag{3}$$

[1] github.com/duembgen/aam_icip18 // infoscience.epfl.ch/record/255464?

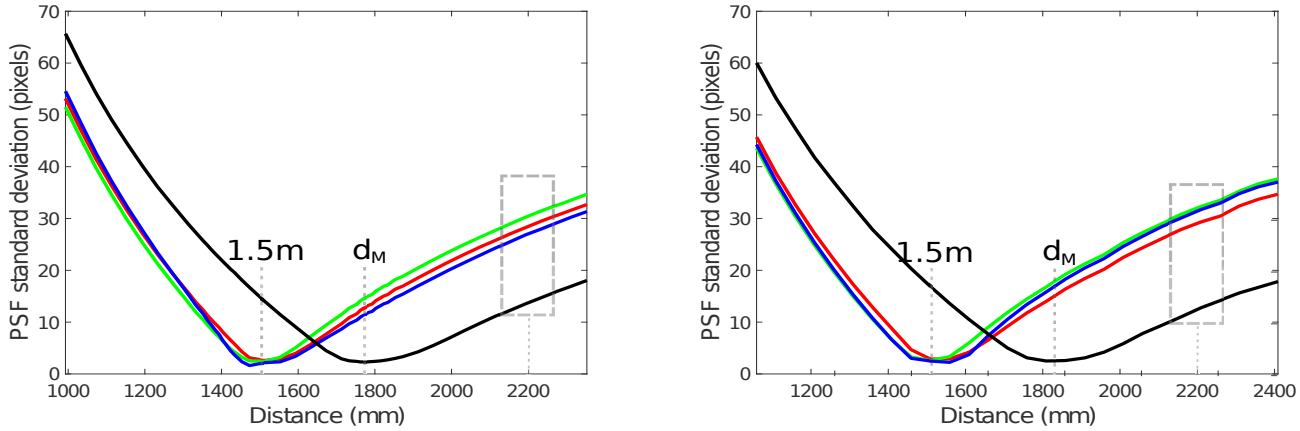

Fig. 3. PSF radius as a function of depth for R, G, B, and NIR, obtained for the lenses: Canon EF 50mm f/2.5 (left) and Canon EF 50mm f/1.8 I (right). The curves are in the corresponding colors for visible bands and in black for NIR. PSF radii are estimated as the standard deviation of a Gaussian curve fitted to the LSF, as explained in Section 2. We can see, for example inside the grey rectangles of equal size on both figures, that the left lens has less axial aberration as the NIR blur is closer to that of the color channels. The difference is harder to visualize between the color channels, but the focal depths are closer to each other for the f/2.5 lens. The shortest-wavelength channel (blue) is focused at 1.5m, and $d_M = x^0_{NIR}$ in our case (Section 4).

where α is a positive parameter smaller than 1 and x^0_i and x^0_j are the focal plane depths for channels Λ_i and Λ_j, respectively. We normalize δ_α to get the average difference:

$$\bar{\delta}_\alpha(\Lambda_i, \Lambda_j) = \frac{1}{b_{ij} - a_{ij}} \int_{a_{ij}}^{b_{ij}} [r_i(x) - r_j(x)]^2 dx. \quad (4)$$

The depth range over which we evaluate the difference between two channels extends around their focal planes. The larger α is, the wider the evaluation range. We intentionally use an asymmetric range around the focal planes to account for the asymmetry of PSF curves (Eq. (6)). The decrease in blur when moving towards the focal depth and away from the camera is faster than its increase when moving beyond the focal depth (Fig. 3). Therefore, the range defined in Eq. (3) is not symmetric with respect to the midpoint between x^0_i and x^0_j, to account for the asymmetry. We thus use a relatively wider range $\alpha * max(x^0_i, x^0_j)$ in the back compared to $\alpha * min(x^0_i, x^0_j)$ in the front. Our AAM metric for a multispectral system acquiring a set of N spectral channels $\{\Lambda_1, ..., \Lambda_N\}$ is given by:

$$AAM_\alpha(\Lambda_1, ..., \Lambda_N) = \log_{10}\left(\frac{1}{|\mathcal{M}|}\sum_{i,j\in M} \bar{\delta}_\alpha(\Lambda_i, \Lambda_j)\right), \quad (5)$$

where $\mathcal{M} = \{i, j \in \mathbb{N} | 1 \leq i < j \leq N\}$ and the operator $|\cdot|$ stands for the cardinality of a set. Different lenses can correct for axial chromatic aberration to different extents at different wavelengths, thus a channel with longer wavelengths could end up focusing at a shallower depth than a channel with a shorter wavelength. For this reason, we evaluate the distance in the PSF curves of every pair of two spectral channels. We lastly normalize by the number of channel pairs to have a fair comparison between multispectral systems with the same band of acquired wavelengths but a different number of acquisition channels.

4. EVALUATION ALGORITHM

To obtain the AAM metric results for a given lens and multispectral system, we apply the following procedure, with the camera placed on a slider:

1- Open the camera aperture to a small f-stop ($\approx$) 2.5, thus magnifying axial chromatic aberration effects by magnifying defocus blur variation with depth. This allows the simulation of large depth ranges with much smaller ones. Smaller apertures (i.e. larger f-stop values) can be used when an f-stop of 2.5 is not an option.

2- Focus the spectral channel with shortest wavelength on a 5-degree slanted edge placed 1.5m away (to have enough margin to get closer), and in the center of the scene.

3- Increase the camera-to-edge distance, *without refocusing the camera*, until the channel with the longest wavelength values is in focus. Call the corresponding distance d_M.

4- Change the camera-to-edge distance from 1m to $1.5{*}d_M$, with uniform steps of 0.05m at most, capturing a photo at every step, also *without refocusing the camera*.

5- Compute the PSF radii at every depth and for every spectral channel as described in Section 2.

6- Compute the AAM metric for varying α values as given by Eq. (9) for the desired group of spectral channels.

For a standard approach that is more robust to Gaussian sampling errors, such as inaccuracies in exact distances of acquisition or in PSF radius estimation, we begin by a least squares fitting of every PSF plot. We choose to fit the curves to a polynomial of degree five as this fitting is easy to integrate, turning the integration into a sum, and is also generalizable to complex lenses obeying different lens blur models. The PSF radius of a lens (assuming a simple lens model) as a function of depth x and wavelength λ is given by:

$$r^{SimpleLens}(x,\lambda) = L\left|1 - \frac{d}{f(\lambda)} + \frac{d}{x}\right|, \tag{6}$$

where the focal length is $f(\lambda)$, L is the aperture radius, and d is the distance between the simple lens and the camera sensor. However, this function is different for more complex cameras with multiple consecutive lenses, hence the utility of using a polynomial fit to estimate the PSF radius as a function of depth. AAM_α can then be simply computed on the polynomial coefficients. The squared difference $[r_i(x) - r_j(x)]^2$ in Eq. (4) can thus be evaluated as:

$$[r_i(x) - r_j(x)]^2 = \sum_{w=0}^{10} d_{ij_w} x^w, \tag{7}$$

where $d_{ij_w} = \sum_{u+v=w} c_{ij_u} c_{ij_v}$, with the set of coefficients $\{c_{ij}\}$ being the difference between the coefficients of $r_i(x)$ and $r_j(x)$, i.e. $\{c_{ij}\}$ are the coefficients of the polynomial $(r_i(x) - r_j(x))$. Substituting Eq. (7) into Eq. (4) results in the average distance between two PSF curves:

$$\bar{\delta}_\alpha(\Lambda_i, \Lambda_j) = \frac{1}{b_{ij} - a_{ij}} \sum_{w=1}^{11} \frac{d_{ij_{w-1}}}{w}(b_{ij}^w - a_{ij}^w), \tag{8}$$

hence $AAM_\alpha(\Lambda_1, ..., \Lambda_N)$

$$= \log_{10}\left(\sum_{i,j \in M} \frac{1}{|\mathcal{M}|}\left(\sum_{w=1}^{11} \frac{d_{ij_{w-1}}(b_{ij}^w - a_{ij}^w)}{w(b_{ij} - a_{ij})}\right)\right), \tag{9}$$

which we compute for multiple camera settings, α values, multispectral bands, and lenses in the following section. Lastly, the values of a_{ij} and b_{ij} depend on x_i^0 and x_j^0 which correspond physically to the camera-object distance with minimal axial-aberration blur for channels Λ_i and Λ_j. We estimate x_i^0 from the polynomially-fitted PSF curves as:

$$x_i^0 = \text{argmin}(r_i(x)). \tag{10}$$

The smaller the AAM value is for a given depth range and multispectral combination, the stronger is the correction of the acquisition system against axial chromatic aberration. The following section reports the results obtained for two consumer lenses and RGB as well as RGB-NIR channels.

5. RESULTS

We follow the procedure presented in Section 4 to compute our AAM metric for different lenses, using a Canon Mark II camera. The AAM is computed for different values of α to assess the aberration magnitude for different scales of depth range in captured scenes. The results are reported in Tables 1 and 2 for the AAM of RGB channels and of RGB-NIR channels, respectively. The NIR channel is acquired by physically replacing the NIR-blocking filter with a visible-light-blocking filter.

Table 1. $AAM_\alpha(R,G,B)$ values as a function of α for two lenses, using an f-stop of 2.5.

α	0.2	0.35	0.5
Canon EF 50mm f/2.5	0.87	1.66	2.34
Canon EF 50mm f/1.8 I	2.97	3.55	4.09

Table 2. $AAM_\alpha(R,G,B,NIR)$ values as a function of α for two lenses, using an f-stop of 2.5.

α	0.2	0.35	0.5
Canon EF 50mm f/2.5	5.59	6.21	6.78
Canon EF 50mm f/1.8 I	5.83	6.44	7.00

We can see that for all lenses and for all spectral channel groups considered, the magnitude of axial chromatic aberration increases the more we move away from the focal plane depths where the channels are most in focus. Indeed, for larger α values, corresponding to a larger depth range of evaluation, the AAM is consistently larger. For shallow capture, a lens with low AAM for small α is desirable for minimal aberration. For capture with deeper scenery, a low AAM for large α is more important. In our case, the Canon EF 50mm f/2.5 is preferable. The opposite is true if high frequency spectral fusion is desired, (e.g. depth-of-field extension or deblurring), where axial aberration can be leveraged [2, 8, 9]. We can visually verify in Fig. 3 that the f/2.5 lens converges the NIR closer to the color bands compared to the f/1.8 lens. The visual verification between color channels is harder to make.

We do not have assessment comparisons with other methods as our approach is, to the best of our knowledge, the first evaluation metric for axial chromatic aberration.

6. CONCLUSION

We introduce a novel assessment metric for lenses. Our AAM metric measures the magnitude of axial chromatic aberration of a lens, between any number of multispectral channels and for different degrees of scene depth range.

The AAM metric is designed to be easily and cheaply reproducible, simply requiring in terms of equipment a slanted edge that can be printed using a regular printer.

7. REFERENCES

[1] E. Allen and S. Triantaphillidou, *The Manual of Photography and Digital Imaging*, CRC Press, 2012.

[2] M. El Helou, Z. Sadeghipoor, and S. Süsstrunk, "Correlation-based deblurring leveraging multispectral chromatic aberration in color and near-infrared joint acquisition," in *Proc. IEEE International Conference on Image Processing (ICIP)*, 2017.

[3] F. A. Jenkins and H. E. White, "Fundamentals of optics," *McGraw-Hill, New York*, p. 51, 1957.

[4] S. Kang, "Automatic removal of chromatic aberration from a single image," in *Proc. IEEE Conference on Computer Vision and Pattern Recognition (CVPR)*, 2007, pp. 1–8.

[5] T. Sun, Y. Peng, and W. Heidrich, "Revisiting cross-channel information transfer for chromatic aberration correction," in *Proc. IEEE Conference on Computer Vision and Pattern Recognition (CVPR)*, 2017, pp. 3248–3256.

[6] J. Korneliussen and K. Hirakawa, "Camera processing with chromatic aberration," *IEEE Transactions on Image Processing*, vol. 23, no. 10, pp. 4539–4552, 2014.

[7] F. Dümbgen, M. El Helou, N. Gucevska, and S. Süsstrunk, "Near-infrared fusion for photorealistic image dehazing," in *IS&T/SPIE Electronic Imaging*, 2018.

[8] Z. Sadeghipoor, Y. M Lu, E. Mendez, and S. Süsstrunk, "Multiscale guided deblurring: Chromatic aberration correction in color and near-infrared imaging," in *23rd European Signal Processing Conference (EUSIPCO)*, 2015, pp. 2336–2340.

[9] O. Cossairt and S. Nayar, "Spectral focal sweep: Extended depth of field from chromatic aberrations," in *Proc IEEE International Conference on Computational Photography (ICCP)*, 2010, pp. 1–8.

[10] P. A. Howarth and A. Bradley, "The longitudinal chromatic aberration of the human eye, and its correction," *Vision Research*, vol. 26, no. 2, pp. 361–366, 1986.

[11] R. Bedford and G. Wyszecki, "Axial chromatic aberration of the human eye," *JOSA*, vol. 47, no. 6, pp. 564_1–565, 1957.

[12] M. Vinas, C. Dorronsoro, D. Cortes, D. Pascual, and S. Marcos, "Longitudinal chromatic aberration of the human eye in the visible and near infrared from wavefront sensing, double-pass and psychophysics," *Biomedical optics express*, vol. 6, no. 3, pp. 948–962, 2015.

[13] M. Nakajima, T. Hiraoka, Y. Hirohara, T. Oshika, and T. Mihashi, "Verification of the lack of correlation between age and longitudinal chromatic aberrations of the human eye from the visible to the infrared," *Biomedical optics express*, vol. 6, no. 7, pp. 2676–2694, 2015.

[14] "Imatest documentation: Chromatic aberration aka color fringing," http://www.imatest.com/docs/sfr_chromatic/, Accessed: 2018-01-17.

[15] "Dxomark measurements for lenses and camera sensors," https://www.dxomark.com/About/In-depth-measurements/Measurements/LCA, Accessed: 2018-01-17.

[16] S. Zhuo and T. Sim, "Defocus map estimation from a single image," *Pattern Recognition*, pp. 1852–1858, 2011.

[17] H. Hu and G. Haan, "Low cost robust blur estimator," in *Proc. IEEE International Conference on Image Processing (ICIP)*, 2006, pp. 617–620.

[18] A. Pentland, T. Darrell, M. Turk, and W. Huang, "A simple, real-time range camera," in *Proc. IEEE Computer Society Conference on Computer Vision and Pattern Recognition (CVPR)*, 1989, pp. 256–261.

[19] J. Elder and S. Zucker, "Local scale control for edge detection and blur estimation," *IEEE Transactions on Pattern Analysis and Machine Intelligence*, pp. 699–716, 1998.

[20] A. Pentland, "A new sense for depth of field," *IEEE Transactions on Pattern Analysis and Machine Intelligence*, pp. 523–531, 1987.

[21] J. Garcia, J. Sanchez, X. Orriols, and X. Binefa, "Chromatic aberration and depth extraction," in *Proc. IEEE International Conference on Pattern Recognition (ICPR)*, 2000, pp. 762–765.

[22] "Resolution and spatial frequency responses," Standard, Photography - Electronic still picture imaging, 2014.